A Hybrid Observer for Localization from Noisy Inertial Data and Sporadic Position Measurements

Filippo D'ippolito, Giovanni Garraffa, Antonino Sferlazza, Luca Zaccarian

A Hybrid Observer for Localization from Noisy Inertial Data and Sporadic Position Measurements

Filippo D'Ippolito[a], Giovanni Garraffa[b], Antonino Sferlazza[a], Luca Zaccarian[c]

[a]*Department of Engineering, University of Palermo, viale delle scienze Ed. 10, 90128 Palermo, Italy. E-mail:* filippo.dippolito@unipa.it, antonino.sferlazza@unipa.it

[b]*Faculty of Engineering and Architecture, University of Enna Kore, 94100 Enna, Italy. E-mail:* giovanni.garraffa@unikore.it

[c]*CNRS, LAAS, Université de Toulouse, 31400 Toulouse, France, and Dipartimento di Ingegneria Industriale, University of Trento, 38122 Trento, Italy. E-mail:* zaccarian@laas.fr

Abstract

We propose an asymptotic position and speed observer for inertial navigation in the case where the position measurements are sporadic and affected by noise. We cast the problem in a hybrid dynamics framework where the continuous motion is affected by unknown continuous-time disturbances and the sporadic position measurements are affected by discrete-time noise. We show that the peculiar hybrid cascaded structure describing the estimation error dynamics is globally finite-gain exponentially ISS with gains depending intuitively on our tuning parameters. Experimental results, as well as the comparison with an Extended Kalman Filter (EKF), confirm the effectiveness of the proposed solution with an execution time two orders of magnitude faster and with a simplified observer tuning because our bounds are an explicit function of the observer tuning knobs.

Keywords: Localization, sampled-data observer, sporadic measurements, hybrid cascaded systems

1. Introduction

Inertial Navigation Systems (INS) Hamel and Mahony (2006); Fossen (2011); Zhang et al. (2012) are gaining increased popularity since they provide a conceptually simple answer to the growing demand of location-based services.

A key aspect for providing safe and reliable autonomous navigation is accurate localization. Indeed, position and velocity estimation using only accelerometers and GPS-like position sensors is an active research field You et al. (2020); Han et al. (2020); Yuan et al. (2021); Qi et al. (2020); Li et al. (2020). Most INSs are based on a 9 Degrees of Freedom (DoF) Inertial Measurement Unit (IMU). IMUs are indeed typically equipped with three accelerometers for the acceleration measurements in the body frame, three gyros for the measurement of the angular velocity vector, referred to as the Earth Centered Inertial (ECI) frame, three magnetometers allowing for attitude estimation. These sensors are commonly fused using the strapdown method Woodman (2007); Zhang et al. (2012); Grip et al. (2013): first transform the body frame accelerometer measurements into inertial frame coordinates, using attitude measurements coming from the estimation of the gravity vector fused with the magnetometers and secondly perform an open-loop double integration to estimate the vehicle position and speed. Due to the noise and sensor biases combined with the open-loop integration of the acceleration signals, drifts in the speed and position estimates must be compensated. Therefore it is well know that IMU-based INS work correctly for short time windows and their behavior degrades rapidly with elapsing time Grip et al. (2013).

To avoid the above-mentioned drift, extra position sensors are typically required alongside the IMU. For example, LIDAR, odometry and/or vision systems are possible high-cost equipment, both in terms of price and computational effort. Odometry is also well-known to be prone for systematic errors (due to sliding and uncertain wheel size), while vision systems could fail in case of poor visibility conditions (darkness, fog,...). For outdoor localization, where satellite signals are accessible, Global Positioning System (GPS) devices are employed. While GPS systems are based on Time-of-Flight (ToF) algorithms, for indoor scenarios different techniques can be used, such as the Received Signal Strength Indicator (RSSI) Feng et al. (2012) and the Time Difference of Arrival (TDoA) measurements Li et al. (2016). The recent surveys Liu et al. (2007); Yassin et al. (2016) describe different technologies and methods for indoor localization.

In this context, one key challenge is to fuse the inertial and position measurements coming from various sensors implementing different technologies and operating at different sampling frequencies (see, e.g., the several works surveyed in Wang and Tayebi (2020)). In this context, Vik and Fossen (2001) presents one of the first nonlinear observers for GPS and IMU sensor data fusion. In Zhao and Slotine (2005), based on contraction theory, a deterministic nonlinear observer is proposed, which takes into account the sampled-data and sporadic nature of the measurements, using additional velocity measurements (not used in this paper). With velocity measurements, a nonlinear observer for inertial navigation is also proposed in Grip et al. (2013). This last work was then extended to time-varying observer gains in Bryne et al. (2014). Similar results relying on velocity measurements are given in Fusini et al. (2014),

which addresses position, velocity and attitude estimation for Unmanned Aerial Vehicles (UAVs).

In this paper we propose a novel estimation strategy, accounting for the sporadic nature of position-only measurements (without velocity sensors) and characterizing the effects of continuous-time process disturbances and discrete-time (sampled) measurement noise. To rigorously represent this scenario, in Section 2 we adopt the hybrid dynamical systems framework of Goebel et al. (2012), which provides an effective and elegant notation, in addition to a number of useful well-posedness results. This hybrid framework has been already used for observers with sporadic measurements enjoying suitable direct and reverse dwell-time constraints on the sampled-data measurement occurrence Ferrante et al. (2016); Li et al. (2018); Sferlazza et al. (2019); Ferrante et al. (2019), due to its suitability for non-periodic sampled-data models. More recent works, such as Bernard and Sanfelice (2022) handle even more challenging situations where the measurement do not satisfy direct or reverse dwell-time constraints and covers, e.g., Zeno solutions as a special cases. While those approaches can solve our estimation problem, the explicit solution developed here takes into account disturbances and noise and is specific to the INS problem setting with an extra dynamical state that allows expressing the bounds on the exponential convergence rate of the estimation error as a function of the tuning knobs of the proposed observer. Indeed, the estimation error dynamics presents a peculiar cascaded structure discussed in Section 3.2. Preliminary results in the direction of this paper have been published in Sferlazza et al. (2020) where we did not take into account external perturbations, nor studied the input-to-state stability properties of our scheme. Indeed, this work generalizes the exponential bounds of Sferlazza et al. (2020) and provides proofs that were omitted in Sferlazza et al. (2020). Moreover, as compared to Sferlazza et al. (2020), our main result stated in Section 3 better characterizes the impact of the observer gains on the exponential rate and ISS gains. Finally, Sferlazza et al. (2020) did not provide experimental results, that we include here in Section 4. We also provide a comparison with an Extended Kalman Filter (EKF), which essentially boils down to being a discrete Kalman filter (without any linearization) with open-loop integration in-between samples for our specific dynamics. It is well-known that EKF designs are associated with nonstrict Lyapunov functions, so that our ISS bound would be nontrivial to obtain with an EKF. Moreover, the persistence of excitation required by the EKF is not required in our design, because it is embedded in our ISS-based proofs. Finally, while comparable performance is obtained with the EKF and our solution, on the same hardware, the EKF execution requires a computational time that is two orders of magnitude larger than our approach.

Notation: $\mathbb{R}^n$ is the n-dimensional Euclidean space. $\mathbb{R}_{\geq 0}$ is the set of nonnegative real numbers. $\mathbb{Z}$ is the set of all integers, while $\mathbb{N}$ is the set of nonnegative integers. I_q is the identity matrix of dimension $q \in \mathbb{N}$, $\mathbf{0}_q$ is a square matrix of dimension $q \in \mathbb{N}$ with all zero elements. $\lambda_m(S)$ and $\lambda_M(S)$ are, respectively, the minimum and the maximum eigenvalues of a symmetric matrix S. $\mathbb{S}^3$ is the 3-sphere $\mathbb{S}^3$. $SO(3) \subset \mathbb{R}^{3\times 3}$ is the special orthogonal group of rotation matrices. x^+ is the state of a hybrid system after a jump. $A^\top$ denotes the transpose of a generic matrix A. $|x|$ is the Euclidean norm of a vector $x \in \mathbb{R}^n$, while $\|\cdot\|_\infty$ denotes the infty norm of a vector $x \in \mathbb{R}^n$. We consider hybrid dynamical systems as in Goebel et al. (2012), whose solutions are defined on *hybrid time-domains*. A subset E of $\mathbb{R}_{\geq 0} \times \mathbb{N}$ is a compact hybrid time-domain if $E = \bigcup_{j=0}^{j_m-1}([t_j, t_{j+1}], j)$ for some finite sequence of times $0 = t_0 \leq t_1 \leq \cdots \leq t_{j_m}$, and it is a hybrid time domain if for any $(t_m, j_m) \in E$, $E \bigcap [0, t_m] \times \{0, \cdots, j_m\}$ is a compact hybrid time domain. For a solution $(t, j) \to x(t, j)$ (see (Goebel et al., 2012, Definition 2.6)), we denote its domain as $\operatorname{dom} x$. For a flowing solution we use $\dot{x}(t, j) = \frac{d}{dt}x(t, j)$ and for jumping solution $x^+(t, j) = x(t, j + 1)$. B, and N denote the BODY and NED (North-East-Down) reference frames, respectively.

2. Sporadic Position Measurements in an Inertial Navigation System

Consider the strap-down model of an Inertial Navigation System (INS) given by: (Bryne et al., 2014, Eq.s (2)-(3)):

$$\dot{\boldsymbol{v}}^n = \boldsymbol{R}\,\boldsymbol{\gamma}^b + \boldsymbol{g} + \boldsymbol{d}, \tag{1}$$

$$\dot{\boldsymbol{p}}^n = \boldsymbol{v}^n, \tag{2}$$

where $\boldsymbol{p}^n := \begin{bmatrix} p_x & p_y & p_z \end{bmatrix}^\top \in \mathbb{R}^3$ and $\boldsymbol{v}^n := \begin{bmatrix} v_x & v_y & v_z \end{bmatrix}^\top \in \mathbb{R}^3$ are respectively the position and velocity vectors expressed in N coordinates (x, y, z), $\boldsymbol{g} := \begin{bmatrix} 0 & 0 & g \end{bmatrix}^\top \in \mathbb{R}^3$ is the gravity acceleration referred to the N-frame, $\boldsymbol{d} \in \mathbb{R}^3$ is a disturbance arising from unmodeled dynamics and unknown external perturbations, $\boldsymbol{\gamma}^b := \begin{bmatrix} \gamma_x & \gamma_y & \gamma_z \end{bmatrix}^\top \in \mathbb{R}^3$ is the acceleration measurement provided by the IMU expressed in the B-frame, and matrix $t \mapsto \boldsymbol{R}(t)$ is a time-varying map from $\mathbb{R}_{\geq 0}$ to $SO(3)$, representing the (time-varying) rotation matrix from the B-frame to the N-frame. The inertial model (1), (2) is obtained under the assumption that the Earth angular velocity about the z-axis of the Earth-Centered Inertial (ECI) frame is small, so that it can be neglected (Grip et al., 2013, Remark 2).

The strap-down inertial navigation algorithm (Zhao and Slotine (2005); Grip et al. (2013)) is not robust, because the speed and the position vectors are obtained by open-loop integration of the acceleration and this leads to drift problems. To solve these observability problems, a position measurement is used, provided by a Global Positioning System (GPS), for outdoor navigation, or beacons, for indoor navigation. Consequently, problems arise because these position measurements are available with a significantly lower sampling rate, as compared to the IMU signals. Moreover the time between two consecutive position measurements is not constant, thus providing a so-called sporadic position measurements situation Ferrante et al. (2019). In order to formalize the above described setting, we assume in this paper that no velocity measurement is available and that the only output of system (1)-(2) is represented by the vector $\boldsymbol{y} \in \mathbb{R}^3$, only accessible at discrete instants of time, resulting in a sequence of 3-dimensional vectors $\boldsymbol{y}_k$, $k \in \mathbb{Z}_{\geq 1}$, defined as:

$$\boldsymbol{y}_k = \boldsymbol{p}_k^n + \boldsymbol{n}_k := \boldsymbol{p}^n(t_k) + \boldsymbol{n}(k), \tag{3}$$

where $\boldsymbol{n}_k \in \mathbb{R}^3$ represents a bounded measurement noise and t_k, $k \in \mathbb{Z}_{\geq 1}$, is a sequence of increasing real numbers that satisfies the following assumption:

Assumption 1. *There exist scalars T_m and T_M, with $0 < T_m \leq T_M$, such that:*

$$T_m \leq t_{k+1} - t_k \leq T_M, \quad \forall\, k \in \mathbb{Z}_{\geq 1}. \tag{4}$$

Assumption 1 requires that the sporadic measurements $\boldsymbol{y}_k$ be available with intersample times lower and upper bounded by positive constants T_m and T_M, whose knowledge is not required by our estimation algorithm. As a consequence, Assumption 1 is extremely mild, ruling out the defective cases of Zeno behaviors (because T_m is greater than zero) and of sporadic measurements available at increasingly rare instants.

Assumption 2. *The measurement noise $\boldsymbol{n}$ and the process disturbance $\boldsymbol{d}$ are bounded. More precisely*

$$\|\boldsymbol{d}\| := \sup_{t \in \mathbb{R}_{\geq 0}} |\boldsymbol{d}(t)| < \infty, \quad \|\boldsymbol{n}\| := \sup_{k \in \mathbb{N}} |\boldsymbol{n}(k)| < \infty. \tag{5}$$

The bounds given in Assumption 2 are reasonable in practical scenarios because $\boldsymbol{n}$ models bounded measurement noise, and $\boldsymbol{d}$ may represent, among other things, a disturbance on the acceleration measurement due to the IMU bias, which is, generally, bounded. A different setting often emerges when an indirect velocity measurement is computed by open-loop integration of the acceleration measurement. In this case, a bounded acceleration measurement bias may result in an unbounded drift error on the (indirect) velocity. Due to this reason, we avoid assuming velocity measurements here.

Using the hybrid systems formalism of Goebel et al. (2012), it is possible to represent the sampled-data system associated with setting (1)–(3) as follows:

$$\begin{cases} \dot{\boldsymbol{v}}^n = \boldsymbol{R}\,\boldsymbol{\gamma}^b + \boldsymbol{g} + \boldsymbol{d}, \\ \dot{\boldsymbol{p}}^n = \boldsymbol{v}^n, \\ \dot{\tau} = 1, \end{cases} \qquad \tau \in [0, T_M], \tag{6a}$$

$$\begin{cases} \boldsymbol{v}^{n+} = \boldsymbol{v}^n, \\ \boldsymbol{p}^{n+} = \boldsymbol{p}^n, \\ \tau^+ = 0, \end{cases} \qquad \tau \in [T_m, T_M], \tag{6b}$$

$$\boldsymbol{y} = \boldsymbol{p}^n + \boldsymbol{n}, \tag{6c}$$

where, the superscript "+" has been defined in the notation section, and timer τ is a state variable keeping track of the elapsed time since the last measurement. Using the proof technique of (Cai et al., 2008, Prop. 1), we obtain that the jump times of a solution satisfy Assumption 1 if and only if the solution satisfies the dwell-time logic enforced by state τ in (6). The flowing and jumping specifications reported in (6a) and (6b) can be written in terms of the so-called *flow set* $\mathcal{C}$ (where continuous motion is allowed) and *jump set* $\mathcal{D}$ (where discrete motion is allowed), defined as

$$(\boldsymbol{v}^n, \boldsymbol{p}^n, \tau) \in \mathcal{C} := \mathbb{R}^3 \times \mathbb{R}^3 \times [0, T_M], \tag{7}$$

$$(\boldsymbol{v}^n, \boldsymbol{p}^n, \tau) \in \mathcal{D} := \mathbb{R}^3 \times \mathbb{R}^3 \times [T_m, T_M]. \tag{8}$$

The impulsive nature of the measurement is represented by the property that $\boldsymbol{y} = \boldsymbol{p}^n + \boldsymbol{n}$ is only available at the jump times. Given the setting above, we may now formalize the main goal of this paper.

Problem 1. *Given plant (6) with output $\boldsymbol{y}$ only available at the sampling times t_k, $k \in \mathbb{Z}_{\geq 1}$ satisfying Assumption 1 and subject to perturbation inputs satisfying Assumption 2, design an asymptotic (hybrid) observer providing a continuous-time estimate $(\hat{\boldsymbol{p}}^n, \hat{\boldsymbol{v}}^n)$ that exponentially converge to the states $(\boldsymbol{p}^n, \boldsymbol{v}^n)$ while ensuring a finite-gain ISS bound from $\|\boldsymbol{d}\|$ and $\|\boldsymbol{n}\|$.*

3. Continuous-Discrete Observer Architecture

3.1. Observer dynamics

To solve Problem 1, we propose an observer providing an asymptotic estimate of the plant state, for any sequence of sampling times t_k at which the sampled output is available, as long as these times satisfy Assumption 1 for some (not known) values of $0 < T_m \leq T_M$. Our observer dynamics does not depend on T_m and T_M and our tuning rules for the observer gains are also independent of these two bounds. Nevertheless, we characterize next (see, among other things, the discussion in Remark 2) that the transient evolution of the estimation error and the ensuing performance depend of T_m and T_M.

The structure of the proposed hybrid observer is:

$$\begin{cases} \dot{\hat{\boldsymbol{v}}}^n = \boldsymbol{R}\,\boldsymbol{\gamma}^b + \boldsymbol{g}, \\ \dot{\hat{\boldsymbol{p}}}^n = \hat{\boldsymbol{v}}^n, \\ \dot{\tau} = 1, \\ \dot{\tilde{\boldsymbol{p}}} = 0, \end{cases} \qquad \tau \in [0,\ T_M], \tag{9a}$$

$$\begin{cases} \hat{\boldsymbol{v}}^{n+} = \hat{\boldsymbol{v}}^n + (1-\alpha_v)\left(\frac{\boldsymbol{y} - \hat{\boldsymbol{p}}^n - \tilde{\boldsymbol{p}}}{\tau}\right), \\ \hat{\boldsymbol{p}}^{n+} = \hat{\boldsymbol{p}}^n + (1-\alpha_p)(\boldsymbol{y} - \hat{\boldsymbol{p}}^n), \\ \tau^+ = 0, \\ \tilde{\boldsymbol{p}}^+ = \alpha_p(\boldsymbol{y} - \hat{\boldsymbol{p}}^n), \end{cases} \qquad \tau \in [T_m,\ T_M], \tag{9b}$$

where $\tilde{\boldsymbol{p}}$ is an auxiliary "zero-order hold" state vector propagating the last position correction term across the intersample interval. Through this variable $\tilde{\boldsymbol{p}}$, the intuition behind the correction term acting on the velocity estimate $\hat{\boldsymbol{v}}^n$ is that of an approximated speed error correction, well captured by the position error divided by the elapsed time τ. More specifically, due to the special structure of dynamics (6), the estimation error for v is constant in-between samples (modulo disturbances), hence it can be computed as the difference between the previous and current position error over the inter-sampling time, which is the intuition behind our sampled-data correction term. Finally, α_v and α_p are two positive gains that may be tuned to suitably adjust the estimation error transient. Note that the measurement $\boldsymbol{y} = \boldsymbol{p}^n + \boldsymbol{n}$ is only used in the jump dynamics of our observer, which is then compliant with the measurement constraints imposed by Assumption 1.

As compared to the architecture used in Alonge et al. (2019), observer (9) considers a different jump map with an extra auxiliary state vector $\tilde{\boldsymbol{p}}$. This extra state is necessary because,

while Alonge et al. (2019) uses simultaneous speed and position measurements, we only have position measurements and a more sophisticated dynamic correction is required. Alternative approaches for this estimation problem can be found in Ferrante et al. (2019); Sferlazza et al. (2019), but they do not comprise the additional state $\tilde{\boldsymbol{p}}$, and their tuning is much more involved due to the lack of an exponential decay guarantee related to the observer gains (α_p and α_v in our case). Our solution is preferable because it exploits the peculiar architecture of the system to provide stronger guarantees.

Remark 1. Note that our observer (9) exploits the following structure of plant (6):

$$\dot{\boldsymbol{p}} = \boldsymbol{v}, \quad \dot{\boldsymbol{v}} = \boldsymbol{\psi} + \boldsymbol{d},$$

where signal $\boldsymbol{\psi}$ is available for measurement. Indeed, the proposed estimation technique could be used in other applications that share the same peculiar structure of the dynamics, where the estimation error for v is constant in-between samples and our peculiar sampled-data correction mechanism (based on a sample-and-hold memory of the past position error) is effective. ⌟

3.2. Error Dynamics and Main Result

Following Problem 1, the main result of this work proves an input-to-state stability bound on the estimation error using the error variables

$$\boldsymbol{e} := \begin{bmatrix} \boldsymbol{e}_v \\ \boldsymbol{e}_p \end{bmatrix} := \begin{bmatrix} \boldsymbol{v}^n \\ \boldsymbol{p}^n \end{bmatrix} - \begin{bmatrix} \hat{\boldsymbol{v}}^n \\ \hat{\boldsymbol{p}}^n \end{bmatrix}, \tag{10a}$$

$$\tilde{\boldsymbol{e}}_v := \boldsymbol{e}_p - \tilde{\boldsymbol{p}} - \tau \boldsymbol{e}_v, \tag{10b}$$

and provides design rules to select the tuning gains α_v and α_p in (9). Note that the error variables in (10) are carefully selected in such a way that, due to the peculiar structure of dynamics (6), in the absence of noise the set where these variables are zero is forward invariant. In particular, the specific choice of $\tilde{e}_v$ ensures that, when the estimation error is zero, then it remains identically zero.

With the error variables (10), the error dynamics issued from (6)-(9) comprises three subsystems, represented in Fig. 1, whose three dynamics are singled out next, even though the variable τ governing the jumps is the same for all of them. The position estimation error dynamics can be written as:

$$\begin{cases} \dot{\boldsymbol{e}}_p = \boldsymbol{e}_v, & \\ \dot{\tau} = 1, & \tau \in [0, T_M], \\ \boldsymbol{e}_p{}^+ = \alpha_p \boldsymbol{e}_p + (\alpha_p - 1)\boldsymbol{n}, & \\ \tau^+ = 0, & \tau \in [T_m, T_M], \end{cases} \tag{11}$$

The speed estimation error dynamics can be written as:

$$\begin{cases} \dot{\boldsymbol{e}}_v = \boldsymbol{d}, & \\ \dot{\tau} = 1, & \tau \in [0, T_M], \\ \boldsymbol{e}_v^+ = \alpha_v \boldsymbol{e}_v + \dfrac{\alpha_v - 1}{\tau}(\tilde{\boldsymbol{e}}_v + \boldsymbol{n}), & \\ \tau^+ = 0, & \tau \in [T_m, T_M]. \end{cases} \tag{12}$$

Finally, the dynamics of $\tilde{\boldsymbol{e}}_v$ is governed by:

$$\begin{cases} \dot{\tilde{\boldsymbol{e}}}_v = -\tau \boldsymbol{d}, & \\ \dot{\tau} = 1, & \tau \in [0, T_M], \\ \tilde{\boldsymbol{e}}_v^+ = -\boldsymbol{n}, & \\ \tau^+ = 0, & \tau \in [T_m, T_M]. \end{cases} \tag{13}$$

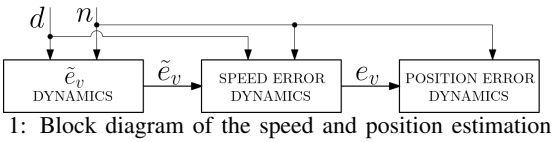

Figure 1: Block diagram of the speed and position estimation error dynamics.

Intuitively speaking, and with reference to Fig. 1, the measurement noise $\boldsymbol{n}$ impulsively affects all three subsystems at the measurement instants (jumps), while the process disturbance $\boldsymbol{d}$ affects the continuous dynamics of the two upper subsystems. The overall dynamics shows a cascaded structure, where, in the absence of noise, the upper subsystem (13) converges to zero in finite time at the first measurement instant; the middle subsystem (12) provides a constant continuous-time behavior in the inter-measurement periods and a discretely converging dynamics (tunable by adjusting α_v) at the measurement instants, perturbed by input $\tilde{\boldsymbol{e}}_v$. Finally, the third subsystem (11) provides a constant continuous-time behavior perturbed by the velocity error $\boldsymbol{e}_v$ in the inter-measurement periods, and a discretely converging dynamics (tunable by adjusting α_p) at the measurement instants. The error dynamics (11)-(13) satisfies the hybrid basic assumptions of (Goebel et al., 2012, Ass. 6.5), indeed the flow and jump sets are closed and the flow and jump maps are continuous in these respective sets.

With error dynamics (11)-(13) our main contribution is to prove an exponential ISS bound where we clarify the role of the tunable observer gains α_p and α_v in (9), thereby providing a solution to Problem 1.

Theorem 1. *Given plant* (1)-(2) *with outputs* (3) *available at measurement times* t_k, $k \in \mathbb{N}$ *satisfying Assumption 1, there exist* $\kappa > 0$ *and* $\lambda > 0$ *such that all solutions to* (11)-(13) *satisfy:*

$$\begin{bmatrix} \boldsymbol{e}_v(t,j) \\ \boldsymbol{e}_p(t,j) \end{bmatrix} \leq \kappa e^{-\lambda t} \left\| \begin{bmatrix} \boldsymbol{e}_v(0,0) \\ \boldsymbol{e}_p(0,0) \\ \tilde{\boldsymbol{e}}_v(0,0) \end{bmatrix} \right\| + \kappa \|\boldsymbol{d}\| + \kappa \|\boldsymbol{n}\|, \tag{14}$$

if and only if the gains α_p *and* α_v *satisfy* $|\alpha_p| < 1$ *and* $|\alpha_v| < 1$. *Moreover, there exist positive constants* γ *and* η, *independent of* α_p *and* α_v, *such that, for any* $\alpha_p \in [0, 1)$ *and* $\alpha_v \in [0, 1)$ *all solutions satisfy*

$$|\boldsymbol{e}_p(t,j)| \leq \frac{\alpha_p^{t/T_M}}{\alpha_p} |\boldsymbol{e}_p(0,0)| + \frac{T_M \alpha_v^{t/T_M}}{(1-\alpha_p)\alpha_v} \left(|\boldsymbol{e}_p(0,0)| + \frac{|\tilde{\boldsymbol{e}}_v(0,0)|}{T_m} \right) + \frac{T_M \gamma}{(1-\alpha_p)(1-\alpha_v)} \|\boldsymbol{d}\| + (\eta + 1)\|\boldsymbol{n}\|, \tag{15}$$

$$|\boldsymbol{e}_v(t,j)| \leq \frac{\alpha_v^{t/T_M}}{\alpha_v} \left(|\boldsymbol{e}_v(0,0)| + \frac{|\tilde{\boldsymbol{e}}_v(0,0)|}{T_M} \right) + \frac{\gamma}{1-\alpha_v} \|\boldsymbol{d}\| + \eta \|\boldsymbol{n}\|. \tag{16}$$

Remark 2. While the necessary and sufficient conditions of Theorem 1 provide a complete characterization of the estimation error dynamics stability, the case of practical interest is $\alpha_p \in [0,1)$ and $\alpha_v \in [0,1)$, because it avoids oscillatory behavior. This case is associated with bounds (16)-(15), providing insight for tuning parameters α_p and α_v and clarifying how the sporadic measurements, as characterized by the minimum and maximum inter-sample times T_m and T_M, affect the localization performance. In particular, first note that the terms $\frac{\alpha^{t/T_M}}{\alpha}$ provide exponential decrease proportional to $\lambda = -\frac{\log(\alpha)}{T_M} > 0$ (positive because $\alpha < 1$) because $\frac{\alpha^{t/T_M}}{\alpha} = \frac{1}{\alpha}e^{-\lambda t}$. Then, choosing a smaller α_p or α_v increases the speed of convergence, but also increases the overshoot, due to the term α at the denominator. A further negative effect occurs with α too large: in addition to slowing down the transient, it undesirably increases the gain from $\|\boldsymbol{d}\|$ and the cascade gain from $|\boldsymbol{e}_v|$ to $|\boldsymbol{e}_p|$. In our experiments we select $\alpha_v = \alpha_p = 0.5$, providing a desirable trade off. ⌟

For proving Theorem 1 we establish input-to-state stability (ISS) Cai and Teel (2009) of the three subsystems of Fig. 1, corresponding to dynamics (11), (12) and (13). In our setting, we may simplify the definitions of Cai and Teel (2009) because our jump and flow sets only depend on the timer τ and our solutions satisfy a dwell-time condition, namely each pair of consecutive jumps is at least T_m continuous-time units apart (see Assupmtion 1). We may then introduce

$$\begin{cases} \dot{x} = f(x,u), \\ \dot{\tau} = 1, \end{cases} \quad \tau \in [0, T_M] \\ \begin{cases} x^+ = g(x,u), \\ \tau^+ = 0, \end{cases} \quad \tau \in [T_m, T_M], \tag{17}$$

where f and g are respectively the flow map and the jump map, functions of the state x and the input u (according with the notation presented in Goebel et al. (2012)), whose solution pairs $((x,\tau),u)$ share the same hybrid time domain $\mathrm{dom}(x) = \mathrm{dom}(u)$. We say that system (17) is finite gain-exponentially input-to-state stable with respect to u if there exist positive scalars κ, λ and γ such that any solution pair of (17) satisfies

$$|x(t,j)| \le \kappa e^{-\lambda t}|x(0,0)| + \gamma\|u\|, \quad \forall (t,j) \in \mathrm{dom}\, x. \tag{18}$$

We first provide three technical lemmas, each of them establishing ISS of the three subsystems (11), (12) and (13), whose proofs are postponed to Section 3.3 to avoid breaking the flow of the exposition.

Lemma 1. *If α_p satisfies $|\alpha_p| < 1$, then the position estimation error dynamics* (11) *is finite-gain exponentially ISS with respect to $\boldsymbol{e}_v$ and $\boldsymbol{n}$. Moreover, when $\alpha_p \in [0,1)$ all solutions satisfy*

$$|\boldsymbol{e}_p(t,j)| \quad \le \quad \frac{\alpha_p^{t/T_M}}{\alpha_p}|\boldsymbol{e}_p(0,0)| \; + \; \frac{T_M}{1-\alpha_p}\|\boldsymbol{e}_v\| \; + \; \|\boldsymbol{n}\|, \tag{19}$$

for all $(t,j) \in \mathrm{dom}\, \boldsymbol{e}_p$.

Lemma 2. *If α_v satisfies $|\alpha_v| < 1$, then the velocity estimation error dynamics* (12) *is finite-gain exponentially ISS with respect to $\tilde{\boldsymbol{e}}_v$, $\boldsymbol{d}$ and $\boldsymbol{n}$. Moreover, when $\alpha_v \in [0,1)$ all solutions satisfy*

$$|\boldsymbol{e}_v(t,j)| \le \frac{\alpha_v^{t/T_M}}{\alpha_v}|\boldsymbol{e}_v(0,0)| + \frac{T_M}{1-\alpha_v}\|\boldsymbol{d}\| + \frac{1}{T_m}\Big(\|\tilde{\boldsymbol{e}}_v\| + \|\boldsymbol{n}\|\Big), \tag{20}$$

for all $(t,j) \in \mathrm{dom}\, \boldsymbol{e}_v$.

Lemma 3. *The $\tilde{\boldsymbol{e}}_v$ dynamics* (13) *is finite-gain exponentially ISS with respect to $\boldsymbol{d}$ and $\boldsymbol{n}$. In particular, for any $\tilde{\alpha} \in (0,1)$ all solutions satisfy*

$$|\tilde{\boldsymbol{e}}_v(t,j)| \quad \le \quad \frac{\tilde{\alpha}^{t/T_M}}{\tilde{\alpha}}|\tilde{\boldsymbol{e}}_v(0,0)| \; + \; T_M^2\|\boldsymbol{d}\| \; + \; \|\boldsymbol{n}\|, \tag{21}$$

for all $(t,j) \in \mathrm{dom}\, \tilde{\boldsymbol{e}}_v$.

With these lemmas we are now ready to prove Theorem 1.

Proof of Theorem 1 Let us first prove necessity of $|\alpha_p| < 1$ and $|\alpha_v| < 1$. Assume that either of them does not hold and focus on the corresponding subsystem (11) or (12) taking a zero initial condition for the preceding subsystem in the cascade connection of Fig. 1, and considering the case when $\boldsymbol{d} = \boldsymbol{n} = 0$. The corresponding dynamics coincides with (17) with $f(x,u) = 0$ and $g(x,u) = \alpha x$, where $|\alpha| \ge 1$. This clearly generates non converging solutions, thus proving that an exponential bound cannot hold. The sufficiency follows by simply concatenating the exponential.

Now we prove the second statement with $\alpha_p \in [0,1)$ and $\alpha_v \in [0,1)$. Concatenating (20) and (21) with $\tilde{\alpha} = \alpha_v$, we get

$$\begin{aligned} |\boldsymbol{e}_v(t,j)| \le & \frac{\alpha_v^{t/T_M}}{\alpha_v}\Big(|\boldsymbol{e}_v(0,0)| + \tfrac{1}{T_m}|\tilde{\boldsymbol{e}}_v(0,0)|\Big) + \\ & + \Big(\tfrac{T_M}{1-\alpha_v} + \tfrac{{T_M}^2}{T_m}\Big)\|\boldsymbol{d}\| + \tfrac{2}{T_m}\|\boldsymbol{n}\|, \end{aligned} \tag{22}$$

which implies (16) with $\gamma = T_M\Big(1 + \frac{T_M}{T_m}\Big)$ and $\eta = \frac{2}{T_m}$ (ensuring $(\frac{T_M}{1-\alpha_v} + \frac{{T_M}^2}{T_m}) \le \frac{\gamma}{1-\alpha_v}$ for any $\alpha_v \in [0,1)$).

Once (16) is proven, we can plug it into (19) to get (15), which completes the proof. □

3.3. Proofs of Lemmas 1, 2 and 3.

Proof of Lemma 1 Consider any state-input solution pair $((\boldsymbol{e}_p,\tau),(\boldsymbol{e}_v,\boldsymbol{n}))$ of (11), and any $(t,k) \in \mathrm{dom}(\boldsymbol{e}_p)$. Since $\dot{\tau} = 1$ and the flow set requires $\tau \le T_M$, we have that $t - t_k \le T_M$, therefore

$$\begin{aligned} \Big|\boldsymbol{e}_p(t,k)\Big| &\le |\boldsymbol{e}_p(t_k,k)| + (t-t_k)\|\boldsymbol{e}_v\|_\infty \\ &\le |\boldsymbol{e}_p(t_k,k)| + T_M\|\boldsymbol{e}_v\|_\infty, \quad \forall t \in [t_k, t_{k+1}]. \end{aligned} \tag{23}$$

In particular, when selecting $(t, j-1) \in \mathrm{dom}(\boldsymbol{e}_p)$ such that $t = t_j$, we may apply (23) with $(t,k) = (t_j, j-1)$ to get

$$\Big|\boldsymbol{e}_p(t_j, j-1)\Big| \le |\boldsymbol{e}_p(t_{j-1}, j-1)| + T_M\|\boldsymbol{e}_v\|_\infty. \tag{24}$$

We continue the proof for the case $\alpha_p > 0$ because similar steps, with less strict exponential bounds, can be followed for $\alpha_p < 0$.

Moreover, at each jump time t_j, $j \geq 1$, we may use the jump equation in (11), combined with (24), to get

$$\begin{aligned}\left|\boldsymbol{e}_p(t_j, j)\right| &\leq \alpha_p |\boldsymbol{e}_p(t_j, j-1)| + |\alpha_p - 1| \|\boldsymbol{n}\|_\infty \\ &\leq \alpha_p |\boldsymbol{e}_p(t_{j-1}, j-1)| + \alpha_p T_M \|\boldsymbol{e}_v\|_\infty + (1-\alpha_p)\|\boldsymbol{n}\|_\infty.\end{aligned}$$

By iterating recursively the above inequalities, we obtain for any $(t, j) \in \mathrm{dom}(\boldsymbol{e}_p)$:

$$\begin{aligned}\left|\boldsymbol{e}_p(t, j)\right| &\leq |\boldsymbol{e}_p(t_j, j)| + T_M \|\boldsymbol{e}_v\|_\infty \\ &\leq \alpha_p^j \left|\boldsymbol{e}_p(t_0, 0)\right| + \textstyle\sum_{i=0}^{j} \alpha_p^i T_M \|\boldsymbol{e}_v\|_\infty \\ &\qquad + \textstyle\sum_{i=1}^{j} \alpha_p^i (1-\alpha_p)\|\boldsymbol{n}\|_\infty \\ &\leq |\alpha_p|^j \left|\boldsymbol{e}_p(0, 0)\right| + \left(\textstyle\sum_{i=0}^{\infty} \alpha_p^i\right)\Big(T_M \|\boldsymbol{e}_v\|_\infty \\ &\qquad + (1-\alpha_p)\|\boldsymbol{n}\|_\infty\Big) \\ &= \alpha_p^j \left|\boldsymbol{e}_p(0, 0)\right| + \tfrac{T_M}{1-\alpha_p}\|\boldsymbol{e}_v\|_\infty + \|\boldsymbol{n}\|_\infty, \end{aligned} \tag{25}$$

where we used $t_0 = 0$ and the sum in the next to last line converges because $0 < \alpha_p < 1$ by assumption.

Due to the fact that solutions to (11) are forced to jump when $\tau = T_M$, it holds for $(t, j) \in \mathrm{dom}(\boldsymbol{e}_p)$ that $j \geq \frac{t}{T_M} - 1$. As a consequence we have $\alpha_p^j \geq \frac{\alpha_p^{t/T_M}}{\alpha_p}$, where we considered the hypothesis $0 < \alpha_p < 1$. By substituting this last inequality in (25), the ISS bound (19) is proven. □

Proof of Lemma 2 Consider any state-input solution pair $((\boldsymbol{e}_v, \tau), (\tilde{\boldsymbol{e}}_v, \boldsymbol{d}, \boldsymbol{n}))$ to (12), and any $(t, k) \in \mathrm{dom}(\boldsymbol{e}_v)$. Since $\dot{\boldsymbol{e}}_v = \boldsymbol{d}$ and $\dot{\tau} = 1$ along flows, and the flow set requires $\tau \leq T_M$, we have that $t - t_k \leq T_M$, therefore we have:

$$\begin{aligned}|\boldsymbol{e}_v(t, k)| &\leq |\boldsymbol{e}_v(t_k, k)| + (t - t_k)\|\boldsymbol{d}\|_\infty \\ &\leq |\boldsymbol{e}_v(t_k, k)| + T_M \|\boldsymbol{d}\|_\infty. \end{aligned} \tag{26}$$

Similar to Lemma 1 we focus on the case $\alpha_v > 0$, because $\alpha_v < 0$ is associated with equivalent derivations. Moreover, at each jump time t_j, $j \geq 1$, we may use the jump equation in (12), combined with (26), and the fact that jumps cannot occur unless $\tau \geq T_m$, to get

$$\begin{aligned}\left|\boldsymbol{e}_v(t_j, j)\right| &\leq \alpha_v |\boldsymbol{e}_v(t_j, j-1)| + \tfrac{1-\alpha_v}{T_m}\Big(\|\tilde{\boldsymbol{e}}_v\|_\infty + \|\boldsymbol{n}\|_\infty\Big) \\ &\leq \alpha_v |\boldsymbol{e}_v(t_{j-1}, j-1)| + \alpha_v T_M \|\boldsymbol{d}\|_\infty \\ &\qquad + \tfrac{1-\alpha_v}{T_m}\Big(\|\tilde{\boldsymbol{e}}_v\|_\infty + \|\boldsymbol{n}\|_\infty\Big).\end{aligned}$$

By iterating the above inequalities, we obtain:

$$\begin{aligned}|\boldsymbol{e}_v(t, j)| &\leq |\boldsymbol{e}_v(t_j, j)| + T_M \|\boldsymbol{d}\|_\infty \\ &\leq \alpha_v^j |\boldsymbol{e}_v(t_0, 0)| + \textstyle\sum_{i=0}^{j} \alpha_v^i T_M \|\boldsymbol{d}\|_\infty \\ &\qquad + \textstyle\sum_{i=1}^{j} \alpha_v^i \tfrac{1-\alpha_v}{T_m}\Big(\|\tilde{\boldsymbol{e}}_v\|_\infty + \|\boldsymbol{n}\|_\infty\Big) \\ &\leq \alpha_v^j |\boldsymbol{e}_v(0, 0)| + \left(\textstyle\sum_{i=0}^{\infty} \alpha_v^i\right)\Big(T_M \|\boldsymbol{d}\|_\infty \\ &\qquad + \tfrac{1-\alpha_v}{T_m}\left(\|\tilde{\boldsymbol{e}}_v\|_\infty + \|\boldsymbol{n}\|_\infty\right)\Big) \\ &= \alpha_v^j |\boldsymbol{e}_v(0, 0)| + \tfrac{T_M}{1-\alpha_v}\|\boldsymbol{d}\|_\infty \\ &\qquad + \tfrac{1}{T_m}\Big(\|\tilde{\boldsymbol{e}}_v\|_\infty + \|\boldsymbol{n}\|_\infty\Big),\end{aligned}$$

where we used $t_0 = 0$ and the sum in the next to last line converges because $|\alpha_v| < 1$ by assumption. The proof is completed as in Lemma 1 to obtain bound (20). □

Proof of Lemma 3 Let us first concentrate on the (possibly zero-length) flowing interval $t_1 - t_0$, to get

$$\begin{aligned}|\tilde{\boldsymbol{e}}_v(t, 0)| &\leq |\tilde{\boldsymbol{e}}_v(0, 0)| + \int_{t_0}^{t} \tau(s, 0)\, |\boldsymbol{d}(s, 0)|\, ds \\ &\leq \tfrac{\tilde{\alpha}^{t/T_M}}{\tilde{\alpha}} |\tilde{\boldsymbol{e}}_v(0, 0)| + {T_M}^2 \|\boldsymbol{d}\|, \forall t \in [t_0, t_1] \end{aligned} \tag{27}$$

where the first term comes from $t - t_0 = t \leq T_M$, namely $\frac{t}{T_M} - 1 \leq 0$ and then $\tilde{\alpha}^{\frac{t}{T_M}-1} \geq 1$, while the second term comes from $t_1 - t_0 \leq T_M$ and $|\tau| \leq T_M$.
Furthermore, from (13), at each jump time (t_j, j), $j \geq 1$, we have $\left|\boldsymbol{e}_v(t_j, j)\right| \leq \|\boldsymbol{n}\|$, which may be used to follow similar steps to those in (27) to get

$$|\tilde{\boldsymbol{e}}_v(t, j)| \leq \|\boldsymbol{n}\| + {T_M}^2 \|\boldsymbol{d}\|, \quad \forall (t, j) \in \mathrm{dom}\, \tilde{\boldsymbol{e}}_v,\ j \geq 1.$$

Combining the bound above with (27), we obtain bound (21), as to be proven. □

4. Experimental validation

4.1. Description of the experimental set-up

The setup, to verify experimentally the proposed observer, is represented in Fig. 2, and consists of the following parts.

The localization system: comprising four fixed beacons (shown at the top-left of Fig. 2) and a mobile beacon mounted on the object to be tracked (top-right of Fig. 2). The beacon hardware is based on a DW1000 IC from Decawave, a single chip IEEE802.15.4-2011 UWB compliant device with internal high precision counter for ToF measurements. Each beacon is equipped with a micro-controller.

The IMU: a LSM9DS1 ST Microelectronics chip that integrates 3 acceleration channels, 3 angular rate channels and 3 magnetic field channels with MEMS technology.

The processing unit: comprising a Raspberry Pi3 core that runs compiled C code generated by the Matlab/Simulink coder, with a 100Hz sampling frequency. The board is based on an ARM Cortex-A53, a 4-CPU 64bit processor running at 1.2Ghz communicating over an I2C bus and a WiFi connection.

The positioning system: a Smart Six-1.4 Comau industrial robot arm, with the mobile beacon placed on the plate secured at the end effector (see the top-right of Fig. 2). The robot imposes a trajectory on the scene, and provides an extremely accurate (encoder-based) position/speed measurement, with a repeatability of 0.05 mm. This accurate position measurement (called "real position/speed" in the following) is not to be used by the observer (except for the illustrative noise-free tests described below), but is used as a ground truth for accurately computing the estimation error and providing an assessment of the observer performance. The robot communicates with the Processing Unit through a wireless UDP.

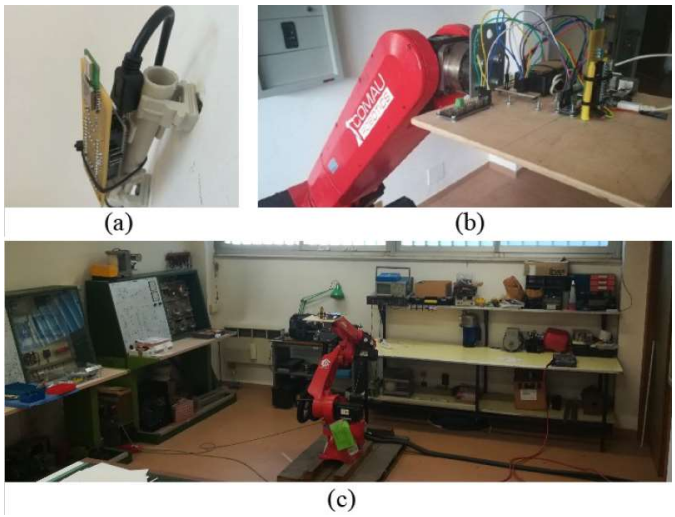

Figure 2: Photo of the experimental setup: (a) fixed beacon, (b) mobile plate to be tracked, (c) indoor scenario.

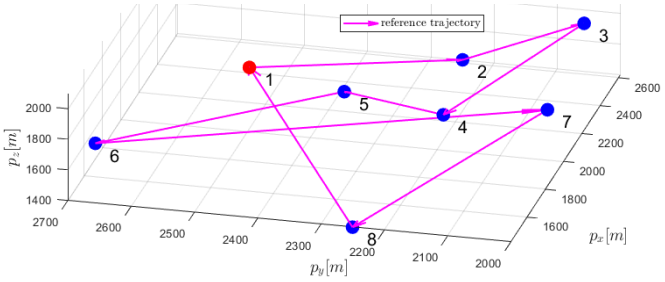

Figure 3: Reference position trajectory.

4.2. Experimental Results

The experimental test consists in actuating the robot in such a way that the plate secured at the end effector tracks a 3D path as in Fig. 3. This link shows a video of the experimental setup: https://www.youtube.com/watch?v=5Z6GOh5jb98. In order to assess the effectiveness of the proposed observer, two tests have been carried out, both of them based on the same experimental trajectory of the plate.

• *Test 1: Noise Free*: The first test (*Test 1*) exploits sampled versions of the accurate (noise free) position measurements provided by the robot internal controller to run the observer in a noise free scenario (the noisy beacons are not used in this first test). This assesses the observer behavior in a noise-free scenario.

• *Test 2: Noisy scenario*: The second test (*Test 2*) runs the observer by only using the IMU data and the noisy position measurements provided by the beacons. The large noise levels of this test allow validating the ISS bounds established in Theorem 1. In this case the noise free position measurements provided by the robot internal controller are only used to compute the estimation error *a posteriori*.

For both tests we focus on sporadic position measurements compliant with Assumption 1 with elapsed time between two consecutive measurements between $T_m = 0.3$s and $T_M = 0.7$s, as shown in Fig. 4. For both tests we tune the observer gains

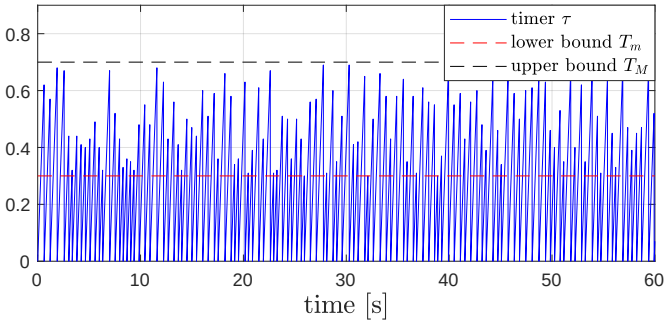

Figure 4: Evolution of the timer variable τ illustrating the interval between each pair of consecutive sampled position measurements.

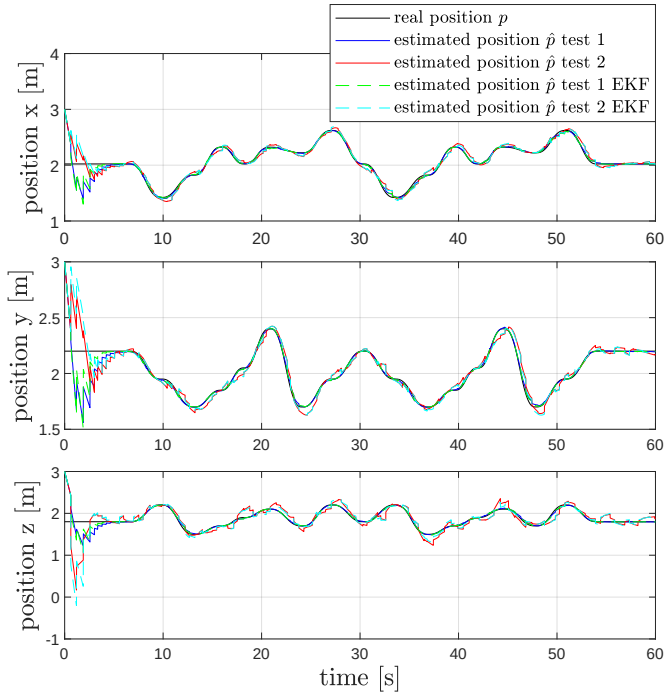

Figure 5: Real and estimated positions for *Test 1* and *Test 2*.

as $\alpha_p = \alpha_v = 0.5$. Finally we also compare the proposed estimation algorithm with the Extended Kalman Filter (EKF) proposed in (Wang and Tayebi, 2020, Algorithm 1) tuned using $G_t V G_t^\top = \left[\begin{array}{c|c} I_3 & \mathbf{0}_3 \\ \hline \mathbf{0}_3 & 0.5 I_3 \end{array}\right]$, $A_t = \left[\begin{array}{c|c} \mathbf{0}_3 & \mathbf{0}_3 \\ \hline I_3 & \mathbf{0}_3 \end{array}\right]$, $P_0 = I_6$, $N_{tk} Q N_{tk}^\top = 0.5 I_3$, (for the symbols, the reader is referred to Wang and Tayebi (2020)), which allow obtaining a similar settling time to the one of our observer, for a meaningful comparison. We emphasize that the EKF solution provides a sound means of comparison but is not associated with the same guarantees as our design, first of all because EKF constructions require proving a persistence of excitation property that is automatically guaranteed by our ISS-based proof, and secondly because the non-strict certificates associated with EKF designs make it hard to extend the obtained bounds to also certify ISS, a property that is instead certified by our bounds, with the additional advantage that the provided bounds are explicit functions of our observer parameters α_p, α_v.

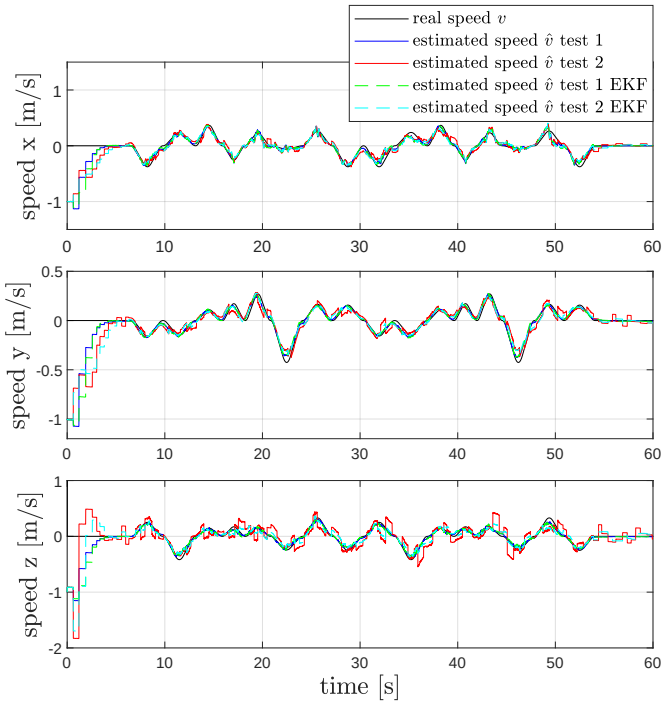

Figure 6: Real and estimated velocities for *Test 1* and *Test 2*.

The results of both tests are shown in Figs. 5 and 6, where the accurate measurements (the "real", ground truth position and speed) based on the robot encoders are shown in black, and the estimated positions and velocities in the x,y and z directions, as obtained from observer (9) and the EKF of Wang and Tayebi (2020), are shown by the colored curves. It is apparent that the estimated variables exponentially converge to the corresponding state variables. Note that the "real" measurements appear very smooth because their accuracy (0.05 mm) is two orders of magnitude smaller than the resolution of our plots. Fig. 7 shows, in logarithmic scale, the position and speed estimation errors for *Test 1* and *Test 2*, when using our observer and the EKF solution of Wang and Tayebi (2020) with a different initial condition associated with a larger initial estimation error. In this case, the logarithmic scale helps best appreciating both the transient and the steady-state errors. The hybrid nature of the estimation is clearly visible in Fig. 7, especially during the initial transient. Indeed, the velocity estimation error is constant during flowing, and decreases across jumps, as expected from the theoretical results, while the position estimation error verifies the ISS bound (19) proven in Lemma 1. The comparison between the blue and red curves of Fig. 7 reveals that *Test 2*, where the observer (9) operates based on the noisy beacon measurements, is associated to significantly larger steady-state estimation errors.

The comparison with the EKF of (Wang and Tayebi, 2020, Algorithm 1), reported in Figs. 5, 6 and 7, shows that both method are valid and exhibit similar performance, in terms of filtering capability. This performance equivalence is quantitatively confirmed by the quantities reported in Table 2, representing the Integral Absolute Error (IAE) indexes computed

	Proposed Observer	EKF
prediction-phase	$0.25\mu s$	$68\mu s$
measurement-update	$0.5\mu s$	$92\mu s$

Table 1: Execution time with the proposed hybrid observer and EKF.

both during the transient $IAE := \frac{1}{t_1}\int_0^{t_1} |\boldsymbol{e}(t)|dt$ and at the steady-state: $IAE := \frac{1}{t_2-t_1}\int_{t_1}^{t_2} |\boldsymbol{e}(t)|dt$, with $t_1 = 6$s and $t_2 = 60$s. For completeness the Integral Time Absolute Error (ITAE) index is shown as well in the same table.

While the performance is comparable, the significant advantage of our observer is found when evaluating the computational effort required by both algorithms. Indeed, the execution time with our observer is two orders of magnitude less than the EKF which makes our solution especially appealing when using low-cost hardware. In particular, for a precise and reliable measurement of the execution times, the two algorithms have been implemented on a Texas dual-core DSP board (TMS320F28379D) design and optimized for real-time control applications, which has a core devoted to (and optimized for) floating point operations. Focusing on the floating point core, we were thus able to measure the algorithms execution times excluding all the supporting tasks (executed by the second core). The comparative results are reported in Table 1 where a significant advantage amounting to more than two orders of magnitude is associated to our application-oriented design. This makes our solution extremely more desirable for situations where low-cost hardware is employed and execution time becomes a cost-sensitive parameter. In addition to this advantage, we recall that the gain tuning for our observer is intuitive and straightforward, due to the explicit effect of gains α_p, α_v on our ISS bounds. Such a simple description is not available for the EKF. Indeed, the persistence of excitation properties, necessary to prove convergence of the EKF, depends on the specific trajectory under consideration (see Huang and Wang (2014); Gaspar and Oliveira (2014) for a more detailed discussion on this aspect). While the error dynamics associated with our application certainly guarantee that property for any trajectory, there is not need to prove this fact with our approach, because we explicitly derive an ISS bound exploiting the (unknown) upper and lower bounds on the inter-sample interval length. We also emphasize that ISS-based proofs are generally hard to obtain with EKF certificates, due to the non-strict Lyapunov functions typically associated with EKF analysis tools.

On the other side one benefit of the EKF is its ability to provide diagnostics coverage in a real-world setting. An observer designer choosing to use an EKF has access to the covariance matrix in addition to the measurement residuals, to note what sensors are the most or least reliable. With the algorithm proposed in this paper, the designer can only rely on the measurement residuals. However, this consideration holds only if the EKF covariance matrices are perfectly known and this is a strong requirement, because the second order statistics of the stochastic processes affecting both the measurements and the dynamics are difficult to determine.

Finally, Fig. 8 shows the estimation errors $\boldsymbol{e}_p$, $\boldsymbol{e}_v$ for differ-

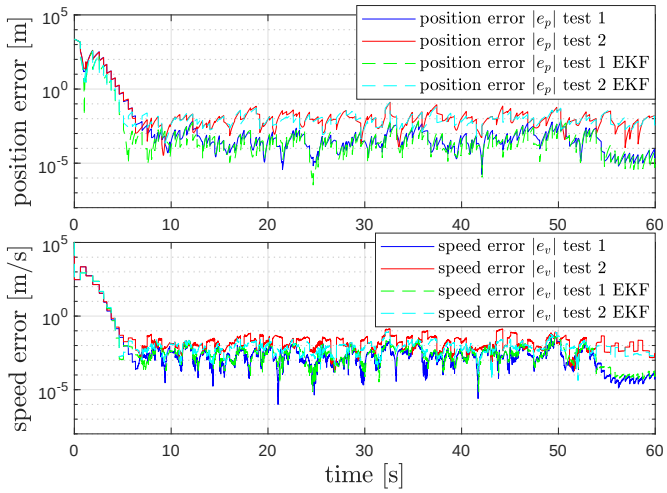

Figure 7: Position errors $\boldsymbol{e}_p$ and velocity errors $\boldsymbol{e}_v$ in *Test 1* and *Test 2*.

ent values of α_p and α_v during *Test 2* (when using the beacon measurements). As one may expect from bounds (15)-(16), the closer α_p and α_v are to zero, the higher the convergence rate of the estimation error. But the higher convergence rate comes at the price of a reduced filtering action on the measurement noise. The choice of α_p and α_v should then be carried out as a trade-off between these two goals. Note that the convergence rate is influenced by the parameters T_m and T_M of the sporadic measurements, as highlighted in Fig. 9, even through the observer dynamics does not require their knowledge. Instead, the increased overshoot predicted by (15)-(16) and commented in Remark 2 cannot be appreciated in the experimental tests.

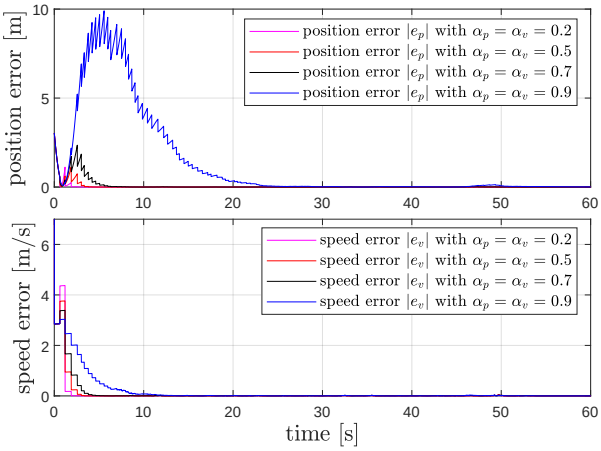

Figure 8: Position and speed errors for different values of α_p and α_v.

5. Conclusions

We proposed a hybrid observation scheme based on a dynamic augmentation to cope with position-only sporadic measurements for inertial navigation. We established finite gain ISS from disturbance inputs and sensor noise to the estimation error. Our ISS bound allows for convenient tuning of the observer gains, which appear explicitly in the bound coefficients.

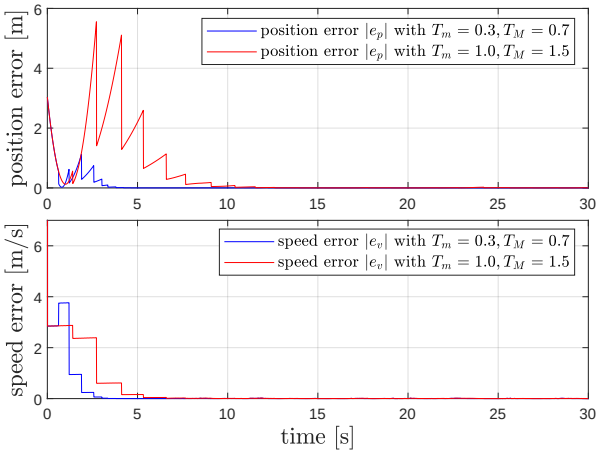

Figure 9: Position and speed errors for different values of T_m and T_M.

Test 1	e_p			e_v		
	IAE_{TR}	IAE_{SS}	$ITAE$	IAE_{TR}	IAE_{SS}	$ITAE$
HYBRID	3.897	1.717	0.107	11.92	3.728	0.2845
EKF	3.558	1.517	0.092	12.71	4.257	0.3085
Test 2	e_p			e_v		
	IAE_{TR}	IAE_{SS}	$ITAE$	IAE_{TR}	IAE_{SS}	$ITAE$
HYBRID	4.616	7.933	0.223	12.94	10.1	0.419
EKF	5.203	7.709	0.235	13.26	7.232	0.3726

Table 2: Steady-state and transient IAE and ITAE indexes for e_p and e_v.

Experiments comparing our solution with a classical EKF show that our observer achieves similar filtering capabilities with a lower computational effort by two orders of magnitude, in addition to being associated with ISS guarantees that are typically hard to obtain with EKF constructions. As a consequence, the proposed solution is attractive when using low-cost hardware.

Acknowledgement

Research supported in part by the Agence Nationale de la Recherche (ANR) via grant "Hybrid And Networked Dynamical sYstems" (HANDY), number ANR-18-CE40-0010 and in part by the MUR under PRIN grant DOCEAT, number 2020RTWES4.

Alonge, F., D'Ippolito, F., Garraffa, G., Sferlazza, A., 2019. A hybrid observer for localization of mobile vehicles with asynchronous measurements. Asian Journal of Control 21, 1506–1521.

Bernard, P., Sanfelice, R., 2022. Observer design for hybrid dynamical systems with approximately known jump times. Automatica 141, 110225.

Bryne, T. H., Fossen, T., Johansen, T. A., 2014. Nonlinear observer with time-varying gains for inertial navigation aided by satellite reference systems in dynamic positioning. In: IEEE Mediterranean Conference on Control and Automation. Palermo, Italy, pp. 1353–1360.

Cai, C., Teel, A., 2009. Characterizations of input-to-state stability for hybrid systems. Systems & Control Letters 58 (1), 47–53.

Cai, C., Teel, A., Goebel, R., 2008. Smooth Lyapunov functions for hybrid systems Part II:(pre) asymptotically stable compact sets. IEEE Transactions on Automatic Control 53 (3), 734–748.

Feng, C., Au, W. S. A., Valaee, S., Tan, Z., 2012. Received-Signal-Strength-Based Indoor Positioning Using Compressive Sensing. IEEE Trans. on Mobile Computing 11 (12), 1983–1993.

Ferrante, F., Gouaisbaut, F., Sanfelice, R. G., Tarbouriech, S., 2016. State estimation of linear systems in the presence of sporadic measurements. Automatica 73, 101–109.

Ferrante, F., Gouaisbaut, F., Sanfelice, R. G., Tarbouriech, S., 2019. $\mathcal{L}_2$ state estimation with guaranteed convergence speed in the presence of sporadic measurements. IEEE Transactions on Automatic Control 64 (8), 3362–3369.

Fossen, T. I., 2011. Handbook of marine craft hydrodynamics and motion control. John Wiley & Sons.

Fusini, L., Fossen, T., Johansen, T. A., 2014. A uniformly semiglobally exponentially stable nonlinear observer for GNSS-and camera-aided inertial navigation. In: IEEE Mediterranean Conference on Control and Automation. Palermo, Italy, pp. 1031–1036.

Gaspar, T., Oliveira, P., 2014. Model-based $\mathcal{H}_2$ adaptive filter for 3D positioning and tracking systems. Automatica 50 (1), 225–232.

Goebel, R., Sanfelice, R. G., Teel, A. R., 2012. Hybrid Dynamical Systems: modeling, stability, and robustness. Princeton University Press.

Grip, H. F., Fossen, T., Johansen, T. A., Saberi, A., 2013. Nonlinear observer for GNSS-aided inertial navigation with quaternion-based attitude estimation. In: American Control Conference. Washington (DC), USA, pp. 272–279.

Hamel, T., Mahony, R., 2006. Attitude estimation on SO(3) based on direct inertial measurements. In: IEEE International Conference on Robotics and Automation. Orlando, FL, USA, pp. 2170–2175.

Han, Y., Wei, C., Li, R., Wang, J., Yu, H., 2020. A novel cooperative localization method based on IMU and UWB. Sensors 20 (2), 467.

Huang, X., Wang, J., 2014. Real-time estimation of center of gravity position for lightweight vehicles using combined AKF-EKF method. IEEE Transactions on Vehicular Technology 63 (9), 4221–4231.

Li, M.-G., Zhu, H., You, S.-Z., Tang, C.-Q., 2020. UWB-based localization system aided with inertial sensor for underground coal mine applications. IEEE Sensors Journal 20 (12), 6652–6669.

Li, X., Deng, Z. D., Rauchenstein, L. T., Carlson, T. J., 2016. Contributed Review: Source-localization algorithms and applications using time of arrival and time difference of arrival measurements. Review of Scientific Instruments 87 (4), 041502.

Li, Y., Phillips, S., Sanfelice, R. G., 2018. Robust distributed estimation for linear systems under intermittent information. IEEE Transactions on Automatic Control 63 (4), 973–988.

Liu, H., Darabi, H., Banerjee, P., Liu, J., 2007. Survey of wireless indoor positioning techniques and systems. IEEE Transactions on Systems, Man, and Cybernetics, Part C 37 (6), 1067–1080.

Qi, Y., Zhong, Y., Shi, Z., 2020. Cooperative 3-D relative localization for UAV swarm by fusing UWB with IMU and GPS. In: Journal of Physics: Conference Series. Vol. 1642. p. 012028.

Sferlazza, A., Tarbouriech, S., Zaccarian, L., 2019. Time-varying sampled-data observer with asynchronous measurements. IEEE Transactions on Automatic Control 64 (2), 869–876.

Sferlazza, A., Zaccarian, L., Garraffa, G., D'Ippolito, F., 2020. Localization from inertial data and sporadic position measurements. In: IFAC World Congress 2020. Berlin, Germany.

Vik, B., Fossen, T., 2001. A nonlinear observer for GPS and INS integration. In: IEEE Conference on Decision and Control. Vol. 3. Orlando, FL, USA, pp. 2956–2961.

Wang, M., Tayebi, A., 2020. Observers design for inertial navigation systems: A brief tutorial. In: IEEE Conference on Decision and Control. Jeju Island, Korea, pp. 1320–1327.

Woodman, O., 2007. An introduction to inertial navigation. Tech. Rep. UCAM-CL-TR-696, University of Cambridge.

Yassin, A., Nasser, Y., Awad, M., Al-Dubai, A., Liu, R., Yuen, C., Raulefs, R., Aboutanios, E., 2016. Recent advances in indoor localization: A survey on theoretical approaches and applications. IEEE Communications Surveys & Tutorials 19 (2), 1327–1346.

You, W., Li, F., Liao, L., Huang, M., 2020. Data fusion of UWB and IMU based on unscented Kalman filter for indoor localization of quadrotor UAV. IEEE Access 8, 64971–64981.

Yuan, S., Wang, H., Xie, L., 2021. Survey on Localization Systems and Algorithms for Unmanned Systems. Unmanned Systems 9 (2), 129–163.

Zhang, W., Ghogho, M., Yuan, B., 2012. Mathematical model and matlab simulation of strapdown inertial navigation system. Modelling and Simulation in Engineering 2012, 1–25.

Zhao, Y., Slotine, J.-J. E., 2005. Discrete nonlinear observers for inertial navigation. Systems & control letters 54 (9), 887–898.